Nano Research

Open Access

Research Article

Modulation of oxygen vacancies and hot electrons promotes highly efficient CO_2 photoreduction towards C_2H_6

Chengyang Zhu[1,§], Hengming Huang[2,§], Huiling Hu[1], Jiaojiao Fang[1] ✉, and Junjie Mao[1] ✉

[1] *Key Laboratory of Functional Molecular Solids, Ministry of Education, College of Chemistry and Materials Science, Anhui Normal University, Wuhu 241002, China*

[2] *College of Materials Science and Engineering, State Key Laboratory of Materials-Orient Chemical Engineering, Jiangsu Collaborative Innovation Center for Advanced Inorganic Function Composites, Jiangsu National Synergetic Innovation Center for Advanced Materials (SICAM), Nanjing Tech University, Nanjing 210009, China*

§ *Chengyang Zhu and Hengming Huang contributed equally to this work.*

Cite this article: *Nano Research*, **2025**, *18*, 94907275. https://doi.org/10.26599/NR.2025.94907275

ABSTRACT: Efficient CO_2 photoreduction towards C_{2+} solar fuels has emerged as one of the most promising strategies for alleviating the current energy and environment problems. However, the C-C coupling barriers and complex multi-electron transfer steps still limit the activity and selectivity of CO_2-to-C_2 photoreduction. Herein, Au nanoparticles (NPs) modified CeO_2 with oxygen vacancies (Au/CeO_2-V_O) were reported for enhancing the CO_2-to-C_2H_6 photoreduction performance. Au/CeO_2-V_O achieved the high C_2H_6 activity of 51.7 μmol·g^{-1}·h^{-1}, accompanied with C_2H_6 selectivity up to 80% in the absence of sacrificial agent. Experimental results combined with theoretical simulation indicated that V_O strengthened CO_2 adsorption and activated *CO production, and plasmon-induced hot electrons from Au NPs to CeO_2-V_O facilitated the *CO-*CO dimerization. The synergistic modulation of V_O and hot electrons further decreased the energy barriers of C-C coupling and subsequent hydrogenation, resulting in the superior photoreduction performance. This work opens an avenue of developing plasmonic photocatalysts for multi-carbon products from CO_2 photoreduction.

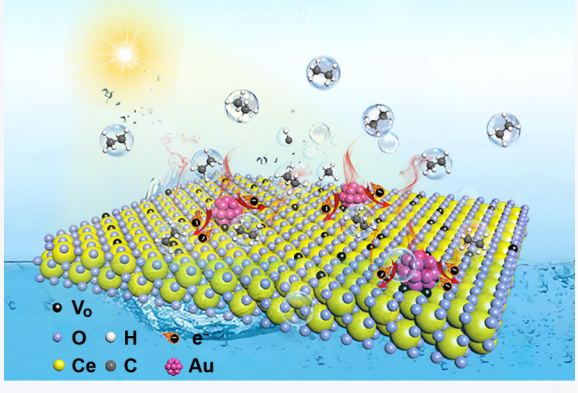

KEYWORDS: synergistic modulation, oxygen vacancy, hot electrons, CO_2 photoreduction, C_2H_6

1 Introduction

Photocatalysis technology, harnessing solar energy to convert CO_2 into hydrocarbons, provides a promising strategy to alleviate the energy and environmental problems [1–5]. The current photocatalytic materials have realized the efficient conversion of CO_2 to C_1 products, such as CO, CH_4, and HCOOH [6–10]. The photoconversion of CO_2 into multi-carbon products, however, not only needs to overcome the high energy barrier of C-C coupling, but also requires plenty of electrons to drive the reaction [11–14]. Owing to the limited electron density generated by solar irradiation, the multi-electron reduction of CO_2 to multi-carbon products is not favor [15–17]. In order to overcome the contradiction between electron density and energy, its deep desirability to develop innovative photocatalytic materials for achieving the efficient photogenerated carriers separation and thereby promoting the conversion of CO_2 into multi-carbon products.

Defect engineering is one of the effective ways to improve charge separation and carrier utilization of intrinsic semiconductor photocatalysts to trigger CO_2 reduction [18–20]. As a typical point defect, oxygen vacancy (V_O) can induce the defect state to capture electrons for enhancing the local electron density [21–24]. Moreover, oxygen vacancy can also regulate the energy band structure of semiconductors and promote the adsorption and activation of CO_2 molecules, which lays the foundation for CO_2 photoconversion [25–28]. Besides the regulation of the electron density in intrinsic semiconductor photocatalysts, the effective injection of external electrons can trigger the supply of multiple electrons on the catalyst surface, which is another way to increase the electron density of catalytic sites [29, 30]. Plasma metal (Au, Ag, Cu, etc.) nanoparticles (NPs) deliver the great potential in the photocatalysis field, due to local surface plasmonic resonance

Received: January 12, 2025; **Revised:** January 26, 2025
Accepted: January 27, 2025

✉Address correspondence to Junjie Mao, maochem@ahnu.edu.cn; Jiaojiao Fang, jjfang@ahnu.edu.cn

(LSPR) effect [31–34]. When the frequency of the incident photon matches the overall vibration frequency of the electrons on the surface of the plasma metal nanoparticles, the collective resonance of free electrons will be generated, which can effectively enhance the light absorption and produce high energy hot electrons [35, 36]. However, the nanoscale metal band gap of zero causes the quick recombination of hot electrons. The composite of plasma metal nanoparticles with semiconductor photocatalysts can effectively induce hot electrons to inject to catalytic sites, inhibit the recombination of hot electrons, and promote electrons/holes separation and transfer [29, 37, 38]. Thus, the combination of vacancy and LSPR effect provides a new opportunity for extracting electrons and manipulating charge carriers to improve the efficiency of multi-electron reaction in CO_2 photoreduction.

Herein, V_O enriched CeO_2 hollow structure supported Au NPs was constructed for elevating the CO_2 photoreduction towards C_2H_6 by the regulation of V_O and hot electrons. The combination of photoelectric characterizations with density functional theory (DFT) simulations indicated that V_O did not only enhance CO_2 absorption, but also favored *CO generation. Moreover, the C-C coupling of *CO intermediates was improved by the plasmon-induced hot electrons from Au NPs to CeO_2-V_O under light irradiation. The energy barriers of the *COCO successive hydrogenation were reduced by the synergy of V_O and hot electrons, which enabled the C_2H_6 production rate of 51.7 $\mu mol \cdot g^{-1} \cdot h^{-1}$, along with high selectivity of 80%.

2 Experimental

2.1 Materials

Cerium nitrate hexahydrate ($Ce(NO_3)_3 \cdot 6H_2O$, > 99.9%) and polyvinylpyrrolidone (PVP, 99%) were purchased from Aladdin and Alfa company, respectively. Cetyltrimethyl ammonium bromide (CTAB, $C_{19}H_{42}BrN$, 99%) was obtained from Aladdin company. Sodium hydroxide (NaOH), chlorauric acid tetrahydrate ($HAuCl_4 \cdot 4H_2O$), ethylene glycol, sodium borohydride ($NaBH_4$) and ethanol were obtained from Sinopharm company. The high purity CO_2 (99.999%) and H_2/Ar (5%/95%) were supplied by Liyuan Gas Company. Ultrapure water (H_2O, 18.2 MΩ·cm) was used in all experiments. All chemicals were used without further purification.

2.2 Synthesis of catalyst

2.2.1 *Preparation of CeO_2*

$Ce(NO_3)_3 \cdot 6H_2O$ (1.0 g) and PVP (0.4 g) were dissolved in ethylene glycol (30 mL) before adding H_2O (1.1 mL). After continuous stirring for 30 min, the obtained clarified solution was transferred to a 100 mL sealed Teflon-lined autoclave and heated at 160 °C for 8 h. After cooling to room temperature, NaOH solution (3 mL, 3 M) was added to the suspension and stirred for 30 min, followed by heating again under 160 °C for 1 h. The product CeO_2 was washed several times by water and ethanol, and finally dried at 60 °C overnight.

2.2.2 *Synthesis of CeO_2-V_O*

150 mg of as-prepared CeO_2 was heated to 500 °C at 5 °C·min^{-1} and kept for 4 h in a 5% H_2/Ar atmosphere to obtained CeO_2 with oxygen vacancies (CeO_2-V_O). CeO_2 with different V_O concentrations were synthesized by changing the calcination temperature and time.

2.2.3 *Fabrication of Au/CeO_2-V_O*

100 mg CeO_2-V_O was dispersed in 24.3 mL H_2O. After the ultrasound treatment for 30 min, 0.5 mL $HAuCl_4$ solution (20 mM) was added, and fully stirred for 2 h to obtain a uniform suspension. Then, 0.2 mL $NaBH_4$ solution (4.3 $g \cdot L^{-1}$) was added to the suspension and stirred vigorously for 6 h. The resulting purple sample (Au/CeO_2-V_O) was washed several times with water and ethanol, and dried at 60 °C overnight. Au/CeO_2-V_O with different Au loading was obtained by changing the content of $HAuCl_4$ added.

2.3 Characterizations

The crystalline structures of samples were characterized on the X-ray diffractometer (XRD, D/MAX-2550) employing Cu Kα radiation. Transmission electron microscopy (TEM, JEOL 200CX) and high-angle annular dark-field scanning TEM (HAADF-STEM, JEOL JEM-ARM 200F) were used to obtain the morphology and crystallography information. The chemical environment and elemental components of samples were analyzed on the Bruker Tensor 22 instrument and Bruker INVENIO R Fourier-transform (FT) spectrometer, X-ray photoelectron spectroscopy (XPS, Ulvac-Phi PHI-5000) and the Beamline 11B of the Shanghai Synchrotron Radiation Facility (SSRF). Raman spectra and N_2 adsorption–desorption isotherms were measured on the RenshawVia Raman spectrometer and Micromeritics ASAP 2460 absorption apparatus, respectively. A Hitachi U-3010 spectrophotometer was performed to analyze the ultraviolet–visible (UV–vis) diffuse reflectance spectra (DRS). Surface photovoltage (SPV) test system (CEL-SPS1000) was used to analyze the surface photovoltage spectra. The photoluminescence (PL) and time-resolved PL (TRPL) spectra were conducted on the fls980 and Horiba Fluomax-4 spectrophotometer, respectively. A gas chromatography-mass spectrometer (GC-MS, Thermo Scientific Trace 1300) was used to record gas products in the $^{13}CO_2$ isotopic labeling experiment. The activated species during reactions and other defects of samples were tested on an electron paramagnetic resonance (EPR) spectrometer (Bruker A300). The CHI 760E electrochemical workstation was used to acquire of the photocurrent responses, electrochemical impedance spectroscopies and Mott–Schottky (M–S) plots.

2.4 Photocatalytic CO_2 reduction reaction (CO_2RR)

Photocatalytic CO_2 reduction experiments were performed in an airtight glassware (50 mL) employing a 300 W xenon lamp as light source. 1.0 mg photocatalyst was dispersed in 0.5 mL ethanol, followed by coating on the quartz glass. The quartz glass was then dried at 60 °C for 30 min and then put in the glassware consisting of 1 mL H_2O. The system removed residual air by pumping CO_2 (> 99.999%). After sealing the glassware, the reaction was conducted for some time. Periodic quantitative analysis of the gaseous product was finally employed on a gas chromatography system (GC9790Plus, Fuli, China) with thermal conductivity detector (TCD) and flame ionization detector (FID) detectors.

3 Results and discussion

3.1 Construction and characterizations of photocatalysts

The Au/CeO_2-V_O was fabricated via a typical two-step method (Fig. 1(a)). The hollow CeO_2 nanoparticles obtained by a

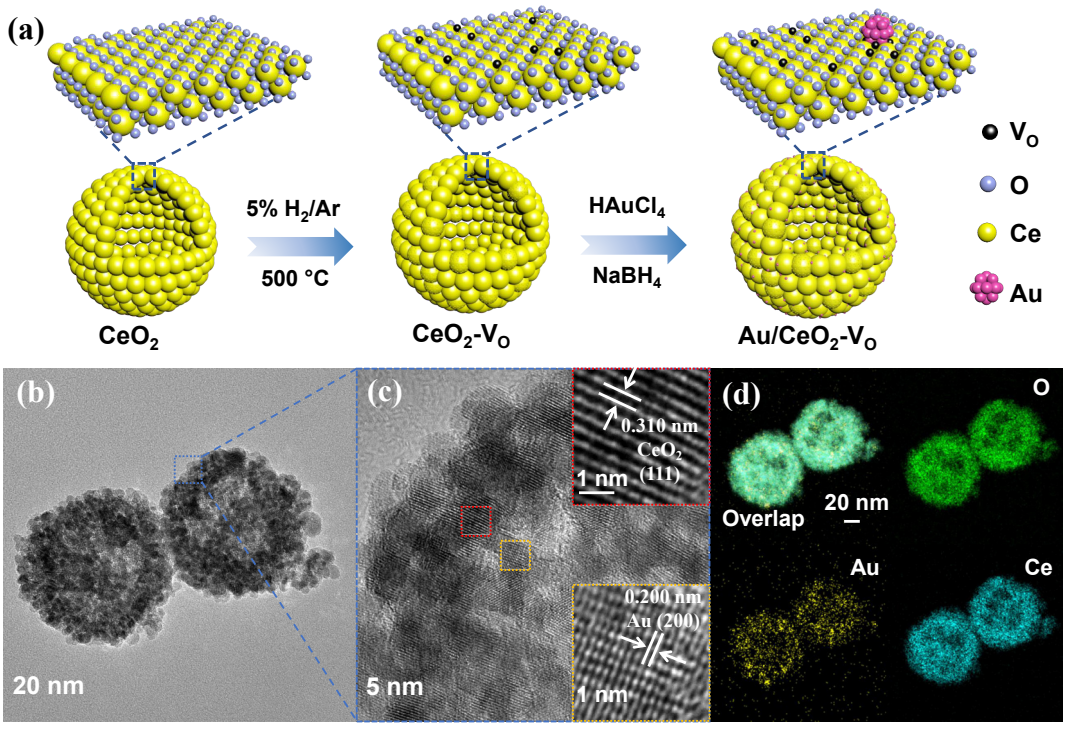

Figure 1 (a) The schematic diagram for the synthetic process of Au/CeO_2-V_O. (b) TEM image, (c) HRTEM image, and (d) elemental mappings of Au/CeO_2-V_O.

hydrothermal process were calcined at high temperature in 5% H_2/Ar to build oxygen vacancies. Subsequently, Au nanoparticles were *in-situ* decorated on the surface through the $NaBH_4$ reduction method to yield Au/CeO_2-V_O. X-ray diffraction patterns of all samples exhibited the almost identical diffraction peaks corresponding to CeO_2 (Fig. S1(a) in the Electronic Supplementary Material (ESM), PDF #43-1002). Moreover, almost no characteristic peaks of Au NPs can be observed, due to their low amount. The presence of Au NPs could be confirmed by Raman spectra, FT infrared (FT-IR) spectra and N_2 adsorption–desorption isotherms (Figs. S1(b)–S1(d) in the ESM). The morphology of Au/CeO_2-V_O was further characterized using transmission electron microscopy and high-resolution TEM image (HRTEM). Au/CeO_2-V_O maintained a hollow spherical structure similar to Au/CeO_2, and Au NPs were evenly distributed on the surface of hollow nanospheres (Figs. 1(b) and 1(c) and Fig. S2 in the ESM). The characteristic lattice spacings of 0.310 and 0.200 nm were indexed to (111) and (200) crystal planes of CeO_2 and Au [25, 32], respectively, indicating the successful introduction of Au NPs on CeO_2-V_O. The energy dispersive X-ray spectroscopy (EDS) images further implied the uniform distribution of Au NPs on CeO_2-V_O (Fig. 1(d)).

The electron paramagnetic resonance technology was conducted to detect the V_O concentration in samples. As Fig. 2(a) depicted, the single Lorentz peak appeared at g = 2.005 was assigned to the free-electrons trapped by V_O, providing evidence for the existence of V_O. The peak intensity of CeO_2-V_O was significantly stronger than that of CeO_2, which revealed the high V_O concentration of CeO_2-V_O. The decreased V_O concentration after introducing Au NPs may be ascribed that Au NPs occupied part of V_O positions. X-ray photoelectron spectroscopy measurement was then employed to determine the surface chemical states of samples. The binding peaks located at 529.1, 530.4, and 531.7 eV in O 1s XPS spectra (Fig. 2(b)) severally belonged to lattice oxygen, V_O and hydroxyl oxygen [20]. Au/CeO_2-V_O endowed an improved V_O ratio with total oxygen compared with Au/CeO_2, consistent with the EPR results. Besides O, the Ce^{3+} content is closely related to the V_O concentration [25]. The peak intensities of Ce^{3+} $3d_{5/2}$ (884.6 eV) and Ce^{3+} $3d_{3/2}$ (903.1 eV) over Au/CeO_2-V_O were stronger than those over Au/CeO_2 (Fig. S3 in the ESM), further disclosing the enhanced content of Ce^{3+} and V_O in Au/CeO_2-V_O. In the Au 4f XPS spectra (Fig. 2(c)), the binding peaks at 83.6 and 97.3 eV were separately attributed to Au $4f_{7/2}$ and Au $4f_{5/2}$ of Au^0 [39], confirming the presence of Au^0 species in samples. Notably, the slight shifts of Au 4f peaks of Au/CeO_2-V_O compared with Au/CeO_2 implied the electron interaction between Au NPs and V_O. To explore the chemical environment of Au species in Au/CeO_2-V_O, we conducted X-ray absorption near-edge structure (XANES) spectroscopy and FT extended X-ray absorption fine structure (FT-EXAFS) measurements. The FT-EXAFS spectra showed that the absorption edge positions of Au/CeO_2-V_O at Au L_3-edge approached to that of Au foil (Fig. 2(d)), suggesting the nearly 0 valence state of Au. The characteristic peak of Au–Au (R = 2.83 Å) was observed on the Au/CeO_2-V_O (Figs. 2(e)–2(g) and Table S1 in the ESM). The close fitting results (Figs. 2(g)–2(i) and Figs. S4 and S5 in the ESM) between Au/CeO_2-V_O and Au foil also verified that Au species mainly existed as Au NPs, matching well with XPS analysis.

3.2 The charge dynamics of photocatalysts

The optical properties of samples were investigated by UV–vis diffuse reflectance spectra. The band edge of CeO_2-V_O exhibited the red shift than that of CeO_2 (Fig. 3(a)). The introduction of Au NPs obviously broadened the light absorption range. The strong LSPR absorption in the 500–600 nm region was observed on both of Au/CeO_2-V_O and Au/CeO_2. Moreover, CeO_2-V_O (2.19 eV) endowed a smaller band gap compared with CeO_2 (2.47 eV, Fig. S6 in the ESM). The band structure alignments of samples were established by analyzing the Mott–Schottky and band gap energy

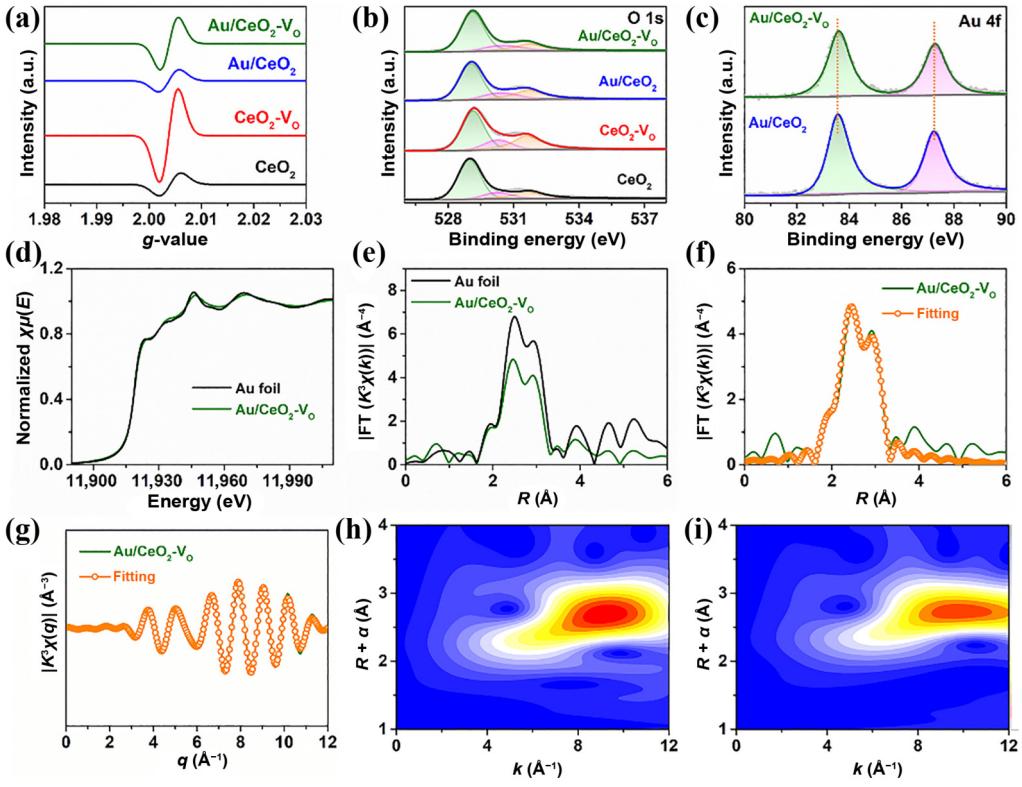

Figure 2 (a) EPR spectra, (b) O 1s, and (c) Au 4f high-resolution XPS spectra of samples. (d) Au L_3-edge XANES spectra, (e) the corresponding FT-EXAFS, (f) *R*-space, and (g) *q*-space fitting curves of Au/CeO_2-V_O. Au L_3-edge wavelet transform (WT)-EXAFS for (h) Au/CeO_2-V_O and (i) Au foil.

plots (Fig. 3(b) and Fig. S6 in the ESM), which were suitable for CO_2 photoreduction. To probe the charge transfer pathway in Au/CeO_2-V_O under light irradiation, we performed the *in-situ* irradiated XPS measurement. The negative shift of the binding energy was observed on Ce 3d XPS spectra (Fig. 3(c)), signifying that Ce atoms acted as the electron acceptors during light irradiation. Meanwhile, the positive shift of the Au binding energy after light irradiation (Fig. 3(d)) indicated the generation and transfer of hot carriers induced by Au NPs LSPR [40]. Moreover, the XPS peak matched to lattice oxygen showed the similar positive shift under light irradiation (Fig. 3(e)). These results revealed the LSPR-induced hot electrons on Au NPs could migrate preferentially to Ce sites of CeO_2-V_O, which may further couple with photogenerated electrons from CeO_2 for enhancing the photocatalytic performance. The surface photovoltage, photocurrent responses, electrochemical impedance spectroscopy (EIS), photoluminescence as well as time-resolved photoluminescence were further employed to discuss the charge dynamics during the photocatalytic reaction. The SPV spectrum of CeO_2 displayed a weak voltage signal that decayed very rapidly (Fig. S7 in the ESM). Compared with CeO_2, CeO_2-V_O has a much high photovoltage signal with long decay time, demonstrating that the improved separation efficiency of photogenerated electron–hole pairs in CeO_2-V_O. Moreover, Au/CeO_2-V_O showed higher photocurrent compared to Au/CeO_2 and CeO_2-V_O (Fig. 3(f)), exhibiting enhanced charge separation by the co-action of Au NPs LSPR and V_O. Additionally, the smallest semicircular radius appeared on Au/CeO_2-V_O (Fig. 3(g)), disclosing that Au/CeO_2-V_O enabled the fastest charge migration rate. Importantly, the PL lifetimes of samples followed the order of Au/CeO_2-V_O (9.62 ns) > Au/CeO_2 (6.56 ns) > CeO_2-V_O (5.54 ns) > CeO_2 (4.74 ns), which was consistent with the results of PL intensities (Figs. 3(h) and 3(i) and Table S2 in the ESM). It further substantiated that the coupling of Au NPs LSPR with V_O greatly inhibited the recombination of photocarriers.

3.3 Photocatalytic CO_2RR performance

The photocatalytic performance of samples towards CO_2 reduction with H_2O was evaluated without any sacrificial agents and photosensitizers. Only CO products were detected on CeO_2 and CeO_2-V_O (Fig. 4(a)). Additionally, the CO yield of CeO_2-V_O (5.8 μmol·g^{-1}·h^{-1}) was higher than that of CeO_2 (2.3 μmol·g^{-1}·h^{-1}), attributing to the V_O effect. After Au NPs deposition on CeO_2-V_O, the yield of C_2H_6 as the primary product attached to 51.7 μmol·g^{-1}·h^{-1} (Fig. 4(b) and Fig. S8 in the ESM), accompanied with 80% selectivity, outperforming the most performance among previously reports (Table S3 in the ESM). Moreover, the C_2H_6 yield of Au/CeO_2-V_O was 32 times as high as that of Au/CeO_2 (1.6 μmol·g^{-1}·h^{-1}), which implied that the coupling of Au NPs LSPR with V_O boosted the CO_2RR performance. Simultaneously, hydrogen gas was not detected in the product (Figs. S9 and S10 in the ESM). Particularly, Au/CeO_2-V_O delivered an elevated apparent quantum efficiency (AQE) of Au/CeO_2-V_O at 520 nm compared with 420 nm (Table S4 in the ESM), further identifying the significant role of hot electrons from LSPR in photocatalysis. Thus, hot electrons from Au NPs LSPR were injected into CeO_2-V_O under the light irradiation of 500–600 nm, while the separation rate of photogenerated carriers in CeO_2-V_O was also elevated by the V_O introduction under < 500 nm light irradiation. The hot electrons coupling with the enhanced photogenerated electrons synergistically promoted the photocatalytic CO_2-to-C_2H_6 performance (Fig. 4(c)). Moreover, no obvious decrease of products

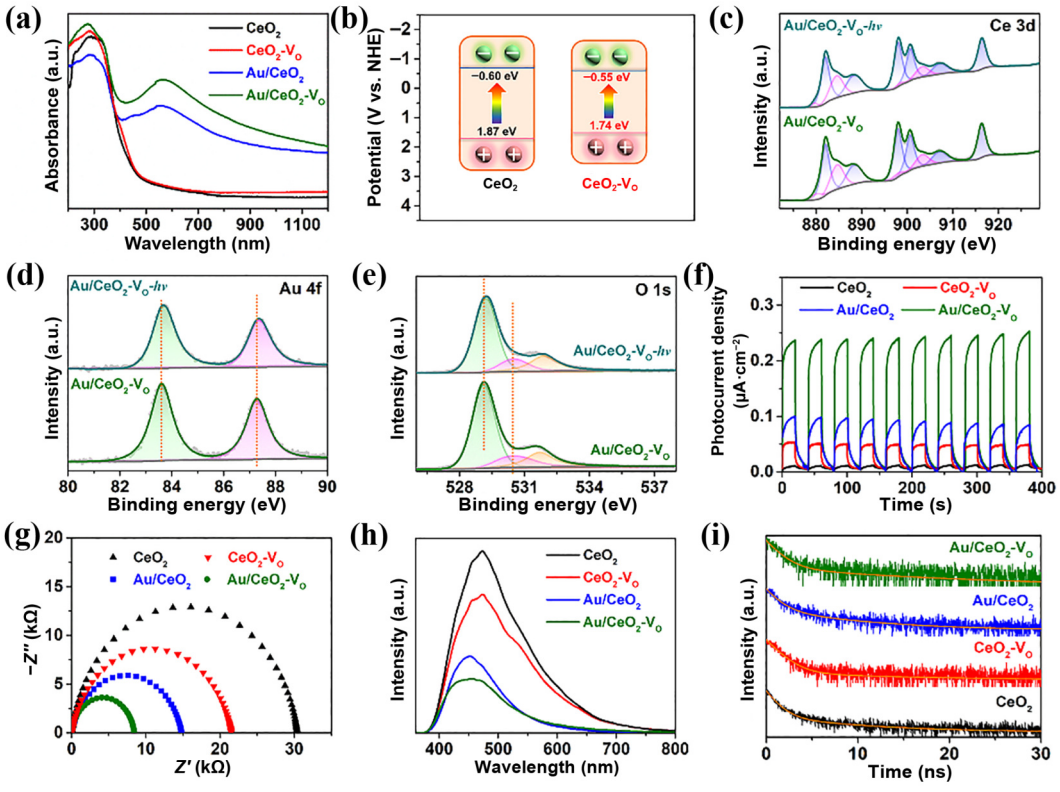

Figure 3 (a) UV–vis DRS of samples. (b) Energy band structures of samples. (c) Ce 3d, (d) Au 4f, and (e) O 1s XPS spectra of Au/CeO_2-V_O before and after light irradiation. (f) Transient photocurrent response, (g) EIS, (h) PL spectra, and (i) TRPL analysis and fitting results of samples.

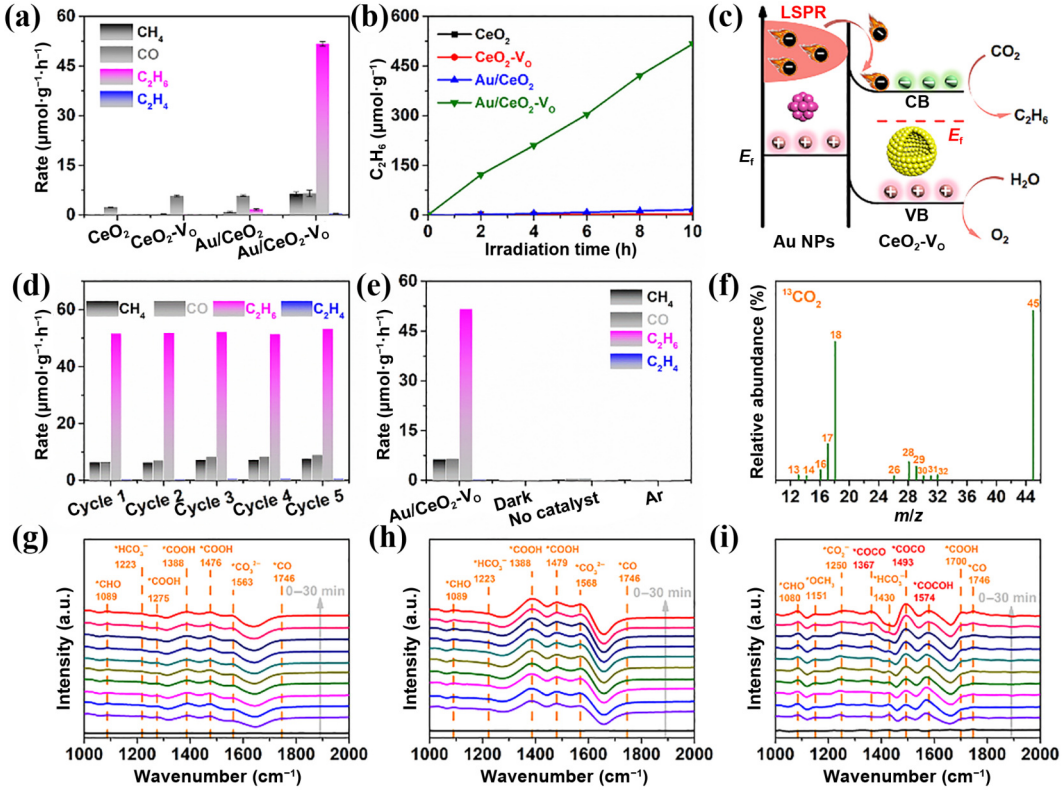

Figure 4 (a) Evolution rates of carbon products over samples. (b) Time-dependent photocatalytic CO_2 reduction to C_2H_6 over samples. (c) The possible mechanism diagram of C_2H_6 products generation process over Au/CeO_2-V_O. (d) The repeated cycles of photocatalytic CO_2RR over Au/CeO_2-V_O. (e) Evolution rates of products over Au/CeO_2-V_O under different conditions. (f) The mass spectrum of product peaks driven from Au/CeO_2-V_O during light irradiation with $^{13}CO_2$ ($^{13}CO_2^+$, m/z = 45; $^{13}C_2H_6^+$, O_2, m/z = 32; $^{13}C_2H_5^+$, m/z = 31; $^{13}C_2H_4^+$, m/z = 30; $^{13}C_2H_3^+$, $^{13}CO_2^+$, m/z = 29; $^{13}C_2H_2^+$, N_2, m/z = 28; $^{13}C_2^+$, m/z = 26; H_2O, m/z = 18; fragments of $^{13}CH_4$, $^{13}CO_2$, N_2 and H_2O, m/z = 13–17). *In-situ* DRIFTS spectra for detecting the reaction intermediates during the photocatalytic CO_2RR over (g) CeO_2, (h) CeO_2-V_O, and (i) Au/CeO_2-V_O.

was observed during five consecutive cycles as indicated by the cycling measurements (Fig. 4(d)), confirmed the excellent stability of Au/CeO_2-V_O. Additionally, the morphology, phase and surface chemical states of Au/CeO_2-V_O were well maintained after cyclic tests (Figs. S11–S13 in the ESM). Control experiments suggested that the negligible product was detected when excluding light condition, the catalyst or CO_2 atmosphere (Fig. 4(e)). Simultaneously, when we replaced Au with Ag and Cu, no C_2H_6 was produced in the photocatalytic CO_2 reduction products for both Ag/CeO_2-V_O and Cu/CeO_2-V_O, further confirming that Au species can effectively promote the generation of C_2H_6. (Fig. S14 in the ESM). The $^{13}CO_2$ isotopic experiment was further used to determine the carbon source of C_2H_6 product. Two characteristic peaks at m/z = 30 and m/z = 31 (Fig. 4(f)) were generated from the fragment ions of $^{13}C_2H_4^+$ and $^{13}C_2H_5^+$, respectively. For the assignment of mass signal at m/z = 32 ($^{13}C_2H_6^+$ or O_2), the CO_2 photoreduction reaction by using $^{12}CO_2$ as raw material was also conducted to avoid the interference of O_2 molecule. The detected signal at m/z = 30 (Fig. S15 in the ESM) corresponds to the $^{12}C_2H_6$ product. These results fully proved that the formed C_2H_6 product derived from the preliminary input CO_2. The *in-situ* diffuse reflectance IR FT spectroscopy (DRIFTS) was studied to explore the reaction intermediates during photocatalytic CO_2RR process. Apart from the similar signals corresponding to *COOH, *CO and *CHO groups on CeO_2 and CeO_2-V_O, the vibration peaks for *OCCO (1367 and 1493 cm^{-1}) and *COCOH (1574 cm^{-1}) intermediates appeared on Au/CeO_2-V_O (Figs. 4(g)–4(i)), indicating the C-C coupling and subsequent hydrogenation processes existed on Au/CeO_2-V_O [41–43]. Specially, the peak intensities of the C-C coupling intermediates over Au/CeO_2-V_O were remarkably higher than those over Au/CeO_2 (Fig. S16 in the ESM), which demonstrated the superior CO_2-to-C_2H_6 photoreduction performance of Au/CeO_2-V_O.

To further verify the effect of V_O and Au NPs LSPR on photocatalysis, samples with different V_O concentrations were prepared by changing the temperature of H_2 treatment (Figs. S17(a) and S17(b) in the ESM). The C_2H_6 activity and selectivity of samples were first increased and then reduced with the increment of V_O concentrations (Fig. S17(c) in the ESM). The optimal performance of photocatalytic CO_2RR was achieved over Au/CeO_2-V_O (500). Using CeO_2-V_O (500) as substrates, Au/CeO_2-V_O with different Au content were prepared and their corresponding photocatalytic CO_2RR activities were characterized. With the Au content improved to 2 wt.%, the C_2H_6 yield was increased to 51.7 $\mu mol \cdot g^{-1} \cdot h^{-1}$, attributing to the positive effect of Au NPs LSPR (Fig. S17(d) in the ESM). The excess introduction of Au could limit the light absorption of CeO_2-V_O and cover the active sites, accordingly weakening the photocatalytic CO_2RR activity.

3.4 Reaction mechanism and theoretical calculations

Density functional theory calculations were performed to describe the underlying mechanism of CO_2-to-C_2H_6 photoreduction on samples. Several obvious impurity states contributed by Ce 4f orbit were observed on the forbidden band of CeO_2-V_O compared with CeO_2 (Figs. 5(a)–5(c)), generating a narrow the bandgap (Fig. S18 in the ESM), which corresponds well with the energy band structures of CeO_2-V_O (Fig. 3(b)). Relative energy diagrams of the CO_2 to CO reaction pathways (Fig. 5(d)) depicted that CO_2 preferred to absorb on CeO_2-V_O. After introducing Au NPs, Au/CeO_2-V_O also exhibited the strong physical adsorption for CO_2/H_2O (Fig. S19 in the ESM). Meanwhile, CO was easily formed and desorpted on CeO_2-V_O compared with CeO_2. After introducing Au NPs, the surface of CeO_2-V_O was more conducive to the CO adsorption (Fig. 5(e)), which was also the premise of the subsequent C-C coupling. The strong charge depletion was observed on Au site, further confirming the electron donor role of Au NPs in Au/CeO_2-V_O (Fig. 5(f)). The absorbed *CO on Au/CeO_2-V_O could couple with another CO to generate *OCCO intermediates. Furthermore, O atom of *COCO on Au/CeO_2-V_O surface was easy to obtain electrons, facilitating the hydrogenation of *COCO to *OCCOH. Obviously, the energies for the subsequent hydrogenation products over Au/CeO_2-V_O were lower than those over Au/CeO_2 (Fig. 5(g) and Fig. S20 in the ESM), which further identified the excellent CO_2-to-C_2H_6 photoreduction performance of Au/CeO_2-V_O.

4 Conclusions

In summary, we reported the Au NPs decorated V_O defective CeO_2 photocatalyst taking advantage of V_O and hot electrons to boost CO_2 photoreduction towards C_2H_6. V_O favored CO_2 absorption and activation for CO, while the efficient injection of hot electrons from Au NPs LSPR into CeO_2-V_O improved the C-C coupling process of *CO intermediates. The modulation of V_O and hot electrons cooperatively lowered the energy barriers of the *COCO formation and subsequent hydrogenation, and facilitated C_2H_6 production. As a result, the optimized photocatalyst delivered an outstanding C_2H_6 yield of 51.7 $\mu mol \cdot g^{-1} \cdot h^{-1}$ with high product selectivity of 80% in the absence of sacrificial agents. This work provides the guidance for designing highly active photocatalysts for efficient CO_2 photoreduction with H_2O to C_2 products.

Electronic Supplementary Material: Supplementary material (the details of apparent quantum efficiency and density functional theory, structural parameters extracted from the Au L_3-edge EXAFS fitting, XRD patterns, Raman spectra, FT-IR spectra and N_2 adsorption–desorption isotherms of sample, TEM, HRTEM of Au/CeO_2, *k*-space curves, *q*-space curves, Mott–Schottky plots, average lifetime results of sample, XRD patterns, TEM, XPS, XANES spectra before and after the repeated cycles of photocatalytic CO_2RR) is available in the online version of this article at https://doi.org/10.26599/NR.2025.94907275.

Data availability

All data needed to support the conclusions in the paper are presented in the manuscript and the Electronic Supplementary Material. Additional data related to this paper may be requested from the corresponding author upon request.

Acknowledgements

This work was supported by the National Natural Science Foundation of China (Nos. 22302002 and 22375006), and the University Science Research Project of Anhui Province (Nos. 2022AH050182 and 2022AH020020). The authors thank the X-ray absorption spectroscopy measurements were performed at Beamline BL11B at the Shanghai Synchrotron Radiation Facility.

Declaration of competing interest

All the contributing authors report no conflict of interests in this work. Author Junjie Mao is the editorial board member of this

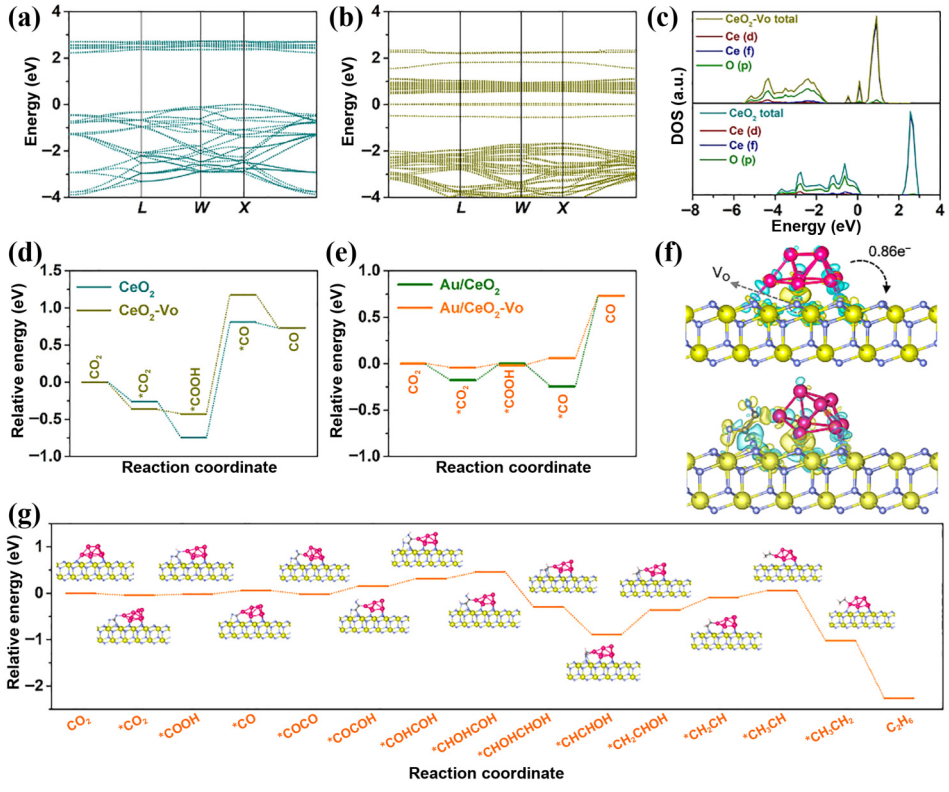

Figure 5 Band structure plots of the simulated (a) CeO_2 and (b) CeO_2-V_O. (c) Band structure plots of the simulated samples. ((d) and (e)) Relative energy diagrams for the suitable pathway of CO_2 to CO on samples. (f) Bader charge analysis of Au/CeO_2-V_O and *OCCO intermediate, where the charge accumulated and depleted regions are shown in yellow and blue, respectively. (g) Relative energy diagram for C_2H_6 formation over Au/CeO_2-V_O, together with the atomic structures of the reaction intermediates.

journal, but he is not involved in the peer-review or decision of this article.

Author contribution statement

C. Y. Z. and J. J. F. designed and engineered the samples, conducted the experiments and data analysis, and wrote the manuscript; J. J. M. performed the data duration and investigation; C. Y. Z. and J. J. F. conceived the idea of this work and revised the manuscript; H. M. H. conducted DFT simulation; H. L. H. revised the manuscript and provided useful advice. All authors contributed to the general discussion. All the authors have approved the final manuscript.

Use of AI statement

None.

References

[1] Zhang, M. R.; Zhang, D.; Jing, X.; Xu, B. J.; Duan, C. Y. Engineering NH_2–Cu–NH_2 triple-atom sites in defective MOFs for selective overall photoreduction of CO_2 into CH_3COCH_3. *Angew. Chem., Int. Ed.* **2024**, *63*, e202402755.

[2] Xie, Z. K.; Xu, S. J.; Li, L. H.; Gong, S. H.; Wu, X. J.; Xu, D. B.; Mao, B. D.; Zhou, T.; Chen, M.; Wang, X. et al. Well-defined diatomic catalysis for photosynthesis of C_2H_4 from CO_2. *Nat. Commun.* **2024**, *15*, 2422.

[3] Wang, L. G.; Wu, J. B.; Wang, S. W.; Liu, H.; Wang, Y.; Wang, D. S. The reformation of catalyst: From a trial-and-error synthesis to rational design. *Nano Res.* **2024**, *17*, 3261–3301.

[4] Fang, J. J.; Zhu, C. Y.; Hu, H. L.; Li, J. Q.; Li, L. C.; Zhu, H. Y.; Mao, J. J. Progress of photocatalytic CO_2 reduction toward multi-carbon products. *Sci. China Chem.* **2024**, *67*, 3994–4013.

[5] Mu, X. Q.; Liu, S. L.; Zhang, M. Y.; Zhuang, Z. C.; Chen, D.; Liao, Y. R.; Zhao, H. Y.; Mu, S. C.; Wang, D. S.; Dai, Z. H. Symmetry-broken Ru nanoparticles with parasitic Ru–Co dual-single atoms overcome the volmer step of alkaline hydrogen oxidation. *Angew. Chem.* **2024**, *136*, e202319618.

[6] Ban, C. G.; Wang, Y.; Feng, Y. J.; Zhu, Z. H.; Duan, Y. Y.; Ma, J. P.; Zhang, X.; Liu, X.; Zhou, K.; Zou, H. J. et al. Photochromic single atom Ag/TiO_2 catalysts for selective CO_2 reduction to CH_4. *Energy Environ. Sci.* **2024**, *17*, 518–530.

[7] Di, J.; Chen, C.; Wu, Y.; Chen, H.; Xiong, J.; Long, R.; Li, S. Z.; Song, L.; Jiang, W.; Liu, Z. Asymmetric electron redistribution in niobic-oxygen vacancy associates to tune noncovalent interaction in CO_2 photoreduction. *Adv. Mater.* **2024**, *36*, 2401914.

[8] Zhang, Y.; Mu, X. Q.; Liu, Z. Y.; Zhao, H. Y.; Zhuang, Z. C.; Zhang, Y. F.; Mu, S. C.; Liu, S. L.; Wang, D. S.; Dai, Z. H. Twin-distortion modulated ultra-low coordination PtRuNi–O_x catalyst for enhanced hydrogen production from chemical wastewater. *Nat. Commun.* **2024**, *15*, 10149.

[9] Tao, Y.; Guan, J. P.; Zhang, J.; Hu, S. Y.; Ma, R. Z.; Zheng, H. R.; Gong, J. X.; Zhuang, Z. C.; Liu, S. J.; Ou, H. H. et al. Ruthenium single atomic sites surrounding the support pit with exceptional photocatalytic activity. *Angew. Chem., Int. Ed.* **2024**, *63*, e202400625.

[10] Wang, L.; Wang, L.; Xu, Y. K.; Sun, G. X.; Nie, W. C.; Liu, L. H.; Kong, D. B.; Pan, Y.; Zhang, Y. H.; Wang, H. et al. Schottky junction and D–A_1–A_2 system dual regulation of covalent triazine frameworks for highly efficient CO_2 photoreduction. *Adv. Mater.* **2024**, *36*, 2309376.

[11] Ning, S. B.; Ou, H. H.; Li, Y. G.; Lv, C. C.; Wang, S. F.; Wang, D. S.; Ye, J. H. Co^0–$Co^{\delta+}$ Interface double-site-mediated C–C coupling for the photothermal conversion of CO_2 into light olefins. *Angew. Chem., Int. Ed.* **2023**, *62*, e202302253.

[12] Zhang, M. Y.; Zhou, D. Y.; Mu, X. Q.; Wang, D. S.; Liu, S. L.; Dai, Z. H. Regulating the critical intermediates of dual-atom catalysts for CO_2 electroreduction. *Small* **2024**, *20*, 2402050.
[13] Fang, J. J.; Zhu, C. Y.; Fang, L. C.; Chen, Y. K.; Hu, H. L.; Wu, Y.; Chen, Q. Q.; Mao, J. J. Efficient charge relay steering in Pd nanoparticles coupled with the heterojunction for boosting CO_2 photoreduction to C_2H_6. *Sci. China Mater.* **2024**, *67*, 2949–2956.
[14] Wang, G.; Chen, Z.; Wang, T.; Wang, D. S.; Mao, J. J. P and Cu dual sites on graphitic carbon nitride for photocatalytic CO_2 reduction to hydrocarbon fuels with high C_2H_6 evolution. *Angew. Chem., Int. Ed.* **2022**, *134*, e202210789.
[15] Xu, R.; Si, D. H.; Zhao, S. S.; Wu, Q. J.; Wang, X. S.; Liu, T. F.; Zhao, H.; Cao, R.; Huang, Y. B. Tandem photocatalysis of CO_2 to C_2H_4 via a synergistic rhenium-(I) bipyridine/copper-porphyrinic triazine framework. *J. Am. Chem. Soc.* **2023**, *145*, 8261–8270.
[16] Wang, G.; Wu, Y.; Li, Z. J.; Lou, Z. Z.; Chen, Q. Q.; Li, Y. F.; Wang, D. S.; Mao, J. J. Engineering a copper single-atom electron bridge to achieve efficient photocatalytic CO_2 conversion. *Angew. Chem., Int. Ed.* **2023**, *62*, e202218460.
[17] Zhang, Y. D.; Sun, Y. J.; Wang, Q. Y.; Zhuang, Z. C.; Ma, Z. T.; Liu, L. M.; Wang, G. M.; Wang, D. S.; Zheng, X. S. Synergy of photogenerated electrons and holes toward efficient photocatalytic urea synthesis from CO_2 and N_2. *Angew. Chem., Int. Ed.* **2024**, *63*, e202405637.
[18] Hu, Q. Y.; Li, M. Q.; Zhu, J. C.; Zhang, Z. X.; He, D. P.; Zheng, K.; Wu, Y.; Fan, M. H.; Zhu, S.; Yan, W. S. et al. Nitrogen doping-roused synergistic active sites in perovskite enabling highly selective CO_2 photoreduction into CH_4. *Nano Lett.* **2024**, *24*, 4610–4617.
[19] Wang, Y.; Ma, F. Y.; Zhang, G. Q.; Zhang, J. W.; Zhao, H.; Dong, Y. M.; Wang, D. S. Precise synthesis of dual atom sites for electrocatalysis. *Nano Res.* **2024**, *17*, 9397–9427.
[20] Yu, J.; Qin, X. T.; Yang, Y. S.; Lv, M. X.; Yin, P.; Wang, L.; Ren, Z.; Song, B. Y.; Li, Q.; Zheng, L. R. et al. Highly stable Pt/CeO_2 catalyst with embedding structure toward water–gas shift reaction. *J. Am. Chem. Soc.* **2024**, *146*, 1071–1080.
[21] Luo, L.; Fu, L.; Liu, H. F.; Xu, Y. X.; Xing, J. L.; Chang, C. R.; Yang, D. Y.; Tang, J. W. Synergy of Pd atoms and oxygen vacancies on In_2O_3 for methane conversion under visible light. *Nat. Commun.* **2022**, *13*, 2930.
[22] Sun, Y. Y.; Ji, H. Q.; Sun, Y. J.; Zhang, G. X.; Zhou, H. J.; Cao, S.; Liu, S. X.; Zhang, L.; Li, W. T.; Zhu, X. W. et al. Synergistic effect of oxygen vacancy and high porosity of nano MIL-125(Ti) for enhanced photocatalytic nitrogen fixation. *Angew. Chem., Int. Ed.* **2024**, *63*, e202316973.
[23] Luo, X.; Zhao, L. X.; Zhou, H. J.; He, L.; Lei, X.; Guan, Q. Q.; Liu, Z. L. Oxygen vacancy induction strategy to regulate the evolution of valence- and free-electrons for boosting visible photodegradation of tetracycline hydrochloride. *J. Hazard. Mater.* **2024**, *466*, 133624.
[24] Liu, B. Y.; Zhang, B. G.; Liu, B. Y.; Hu, Z. F.; Dai, W. J.; Zhang, J. R.; Feng, F. D.; Lan, B.; Zhang, T.; Huang, H. B. Surface hydroxyl and oxygen vacancies engineering in ZnSnAl LDH: Synergistic promotion of photocatalytic oxidation of aromatic VOCs. *Environ. Sci. Technol.* **2024**, *58*, 4404–4414.
[25] Yang, S. Y.; Zhang, W. S.; Pan, G. L.; Chen, J. Y.; Deng, J. Y.; Chen, K.; Xie, X. L.; Han, D. X.; Dai, M. J.; Niu, L. Photocatalytic Co-reduction of N_2 and CO_2 with CeO_2 catalyst for urea synthesis. *Angew. Chem., Int. Ed.* **2023**, *62*, e202312076.
[26] Tang, Z.; Li, Y. J.; Zhang, K. X.; Wang, X. X.; Wang, S. Y.; Sun, Y. F.; Zhang, H. Y.; Li, S. Y.; Wang, J. R.; Gao, X. Y. et al. Interfacial hydrogen spillover on Pd–TiO_2 with oxygen vacancies promotes formate electrooxidation. *ACS Energy Lett.* **2023**, *8*, 3945–3954.
[27] Han, W.; Chen, Y. J.; Jiao, Y. Z.; Liang, S. M.; Li, W.; Tian, G. H. Oxygen vacancy-rich S-scheme CeO_2@$Ni_{1-x}Co_xSe_2$ hollow spheres derived from NiCo–MOF for remarkable photocatalytic CO_2 conversion. *ACS Sustain. Chem. Eng.* **2023**, *11*, 7787–7797.
[28] Hao, L.; Huang, H. W.; Zhang, Y. H.; Ma, T. Y. Oxygen vacant semiconductor photocatalysts. *Adv. Funct. Mater.* **2021**, *31*, 2100919.
[29] Hou, T. L.; Li, X. Y.; Zhang, X. M.; Cai, R. S.; Wang, Y. C.; Chen, A. K.; Gu, H. F.; Su, M. Y.; Li, S. Y.; Li, Q. Z. et al. Atomic Au_3Cu palisade interlayer in core@shell nanostructures for efficient Kirkendall effect mediation. *Nano Lett.* **2024**, *24*, 2719–2726.
[30] Shangguan, W. C.; Liu, Q.; Wang, Y.; Sun, N.; Liu, Y.; Zhao, R.; Li, Y. X.; Wang, C. Y.; Zhao, J. C. Molecular-level insight into photocatalytic CO_2 reduction with H_2O over Au nanoparticles by interband transitions. *Nat. Commun.* **2022**, *13*, 3894.
[31] Jiang, J. W.; Wang, X. F.; Guo, H. Enhanced interfacial charge transfer/separation by LSPR-induced defective semiconductor toward high CO_2RR performance. *Small* **2023**, *19*, 2301280.
[32] Li, X. Y.; Li, C.; Xu, Y. X.; Liu, Q.; Bahri, M.; Zhang, L. Q.; Browning, N. D.; Cowan, A. J.; Tang, J. W. Efficient hole abstraction for highly selective oxidative coupling of methane by Au-sputtered TiO_2 photocatalysts. *Nat. Energy* **2023**, *8*, 1013–1022.
[33] Zhang, S. C.; Chen, D.; Chen, P. G.; Zhang, R.; Hou, Y.; Guo, Y.; Li, P.; Liang, X.; Xing, T. Y.; Chen, J. et al. Concurrent mechanisms of hot electrons and interfacial water molecule ordering in plasmon-enhanced nitrogen fixation. *Adv. Mater.* **2024**, *36*, 2310776.
[34] Zhao, J. Q.; Bai, Y.; Li, Z. H.; Liu, J. J.; Wang, W.; Wang, P.; Yang, B.; Shi, R.; Waterhouse, G. I. N.; Wen, X. D. et al. Plasmonic Cu nanoparticles for the low-temperature photo-driven water–gas shift reaction. *Angew. Chem., Int. Ed.* **2023**, *62*, e202219299.
[35] Tang, J. L.; Li, Y. L.; Ye, S.; Jiang, P. Z.; Xue, Z. H.; Li, X. F.; Lyu, X. Y.; Liu, Q. Y.; Chu, S. S.; Yang, H. et al. Direct hot-electron transfer at the Au nanoparticle/monolayer transition-metal dichalcogenide interface observed with ultrahigh spatiotemporal resolution. *Nano Lett.* **2024**, *24*, 2931–2938.
[36] Dey, A.; Mendalz, A.; Wach, A.; Vadell, R. B.; Silveira, V. R.; Leidinger, P. M.; Huthwelker, T.; Shtender, V.; Novotny, Z.; Artiglia, L. et al. Hydrogen evolution with hot electrons on a plasmonic-molecular catalyst hybrid system. *Nat. Commun.* **2024**, *15*, 445.
[37] Meng, L. J.; How, Z. T.; Chelme-Ayala, P.; Benally, C.; Gamal El-Din, M. Z-scheme plasmonic Ag decorated Bi_2WO_6/NiO hybrids for enhanced photocatalytic treatment of naphthenic acids in real oil sands process water under simulated solar irradiation. *J. Hazard. Mater.* **2023**, *454*, 131441.
[38] Jiang, W. C.; Deng, Y. H.; Su, R.; Xu, J. P.; Liu, L. High-detectivity and broadband MoS_2 phototransistor array by coupling negative capacitance and local surface plasmon resonance effects. *ACS Photonics* **2024**, *11*, 2308–2315.
[39] Wu, W. L.; Zhang, N.; Wang, Y. H. Construction of Au/$ZnWO_4$/CdS ternary photocatalysts with oxygen vacancy modification for efficient photocatalytic hydrogen production. *Adv. Funct. Mater.* **2024**, *34*, 2316604.
[40] Tsao, C. W.; Narra, S.; Kao, J. C.; Lin, Y. C.; Chen, C. Y.; Chin, Y. C.; Huang, Z. J.; Huang, W. H.; Huang, C. C.; Luo, C. W. et al. Dual-plasmonic Au@Cu_7S_4 yolk@shell nanocrystals for photocatalytic hydrogen production across visible to near infrared spectral region. *Nat. Commun.* **2024**, *15*, 413.
[41] Wang, W.; Deng, C. Y.; Xie, S. J.; Li, Y. F.; Zhang, W. Y.; Sheng, H.; Chen, C. C.; Zhao, J. C. Photocatalytic C–C coupling from carbon dioxide reduction on copper oxide with mixed-valence copper(I)/copper(II). *J. Am. Chem. Soc.* **2021**, *143*, 2984–2993.
[42] Ren, L. T.; Yang, X. N.; Sun, X.; Wang, Y. L.; Li, H. Q.; Yuan, Y. P. Cascaded *CO–*COH intermediates on a nonmetallic plasmonic photocatalyst for CO_2-to-C_2H_6 with 90.6% selectivity. *Angew. Chem., Int. Ed.* **2024**, *63*, e202404660.
[43] Wang, J. Y.; Yang, C.; Mao, L.; Cai, X. Y.; Geng, Z. K.; Zhang, H. Y.; Zhang, J. Y.; Tan, X.; Ye, J. H.; Yu, T. Regulating the metallic Cu–Ga bond by S vacancy for improved photocatalytic CO_2 reduction to C_2H_4. *Adv. Funct. Mater.* **2023**, *33*, 2213901.